Simple imaging protocol for autofluorescence elimination and optical sectioning in fluorescence endomicroscopy

Ruikang Zhang, Raja Chouket, Alison G Tebo, Marie-Aude Plamont, Zsolt Kelemen, Lionel Gissot, Jean-Denis Faure, Arnaud Gautier, Vincent Croquette, Ludovic Jullien, et al.

optica

Simple imaging protocol for autofluorescence elimination and optical sectioning in fluorescence endomicroscopy

Ruikang Zhang,[1,†] Raja Chouket,[1,†] Alison G. Tebo,[1] Marie-Aude Plamont,[1] Zsolt Kelemen,[2] Lionel Gissot,[2] Jean-Denis Faure,[2] Arnaud Gautier,[1] Vincent Croquette,[3,4,5] Ludovic Jullien,[1,6] and Thomas Le Saux[1,7]

[1]PASTEUR, Département de Chimie, École normale supérieure, PSL University, Sorbonne Université, CNRS, 75005 Paris, France
[2]Institut Jean-Pierre Bourgin, INRA, AgroParisTech, CNRS, Saclay Plant Sciences (SPS), UniversitéParis-Saclay, Versailles, France
[3]Laboratoire de Physique Statistique, École normale supérieure, PSL Research University, Université Paris Diderot Sorbonne Paris-Cité, Sorbonne Université, CNRS, 75005 Paris, France
[4]Institut de biologie de l'École normale supérieure (IBENS), École normale supérieure, CNRS, INSERM, PSL Research University, 75005 Paris, France
[5]e-mail: vincent.croquette@ens.fr
[6]e-mail: ludovic.jullien@ens.fr
[7]e-mail: thomas.lesaux@ens.fr

Fiber-optic epifluorescence imaging with one-photon excitation benefits from its ease of use, cheap light sources, and full-frame acquisition, which enables it for favorable temporal resolution of image acquisition. However, it suffers from a lack of robustness against autofluorescence and light scattering. Moreover, it cannot easily eliminate the out-of-focus background, which generally results in low-contrast images. In order to overcome these limitations, we have implemented fast out-of-phase imaging after optical modulation (Speed OPIOM) for dynamic contrast in fluorescence endomicroscopy. Using a simple and cheap optical-fiber bundle-based endomicroscope integrating modulatable light sources, we first showed that Speed OPIOM provides intrinsic optical sectioning, which restricts the observation of fluorescent labels at targeted positions within a sample. We also demonstrated that this imaging protocol efficiently eliminates the interference of autofluorescence arising from both the fiber bundle and the specimen in several biological samples. Finally, we could perform multiplexed observations of two spectrally similar fluorophores differing by their photoswitching dynamics. Such attractive features of Speed OPIOM in fluorescence endomicroscopy should find applications in bioprocessing, clinical diagnostics, plant observation, and surface imaging. © 2019 Optical Society of America under the terms of the OSA Open Access Publishing Agreement

https://doi.org/10.1364/OPTICA.6.000972

1. INTRODUCTION

Fiber-optic-based fluorescence endomicroscopes are versatile devices that have found numerous biological and medical applications [1–5]. In contrast to conventional imaging tools, they permit the non-invasive imaging of cells when they are located within hollow tissue tracts or deeply embedded within solid organs [6]. They are also convenient to observe poorly accessible samples such as plant roots in soil [7,8]. They have been widely implemented to facilitate the observation of the brain of freely moving animals [9].

Various strategies arising from microscopy (including confocal, multi-photon, and structured illumination imaging [10–12]) have been transposed in fiber-bundle endomicroscopy in order to deal with optical sectioning. In confocal microscopes, the axial resolution of the system strongly relies on the use of both high-numerical-aperture (NA) objectives to image the specimen and a pinhole of small diameter, which selects for the collection of fluorescence emission at the focal plane. In fiber-bundle-based endoscopes, confocal scanning is performed at the proximal end of the fiber bundle, and a single fiber core acts as both a point-like excitation source and a pinhole. With typical core size around 5 μm and NA of the fiber of 0.4, the axial fluorescence intensity decays only slowly out of the focal plan and lessens the confinement of the collected fluorescence [10,12–14]. To improve the sectioning ability, additional high-NA objectives have been used to tightly refocus the excitation beam exiting from the fiber onto the specimen [15,16]. While efficient, these approaches require specialized optics for the endoscope. Whereas confocal detection eliminates the background caused by out-of-focus light and scatter by introducing a spatial filter along the optical pathway, multi-photon-excited fluorescence imaging overcomes this limitation by restricting significant fluorescence emission to the focus of the light source [12,17,18]. However, the laser pulses necessitated by multiphoton excitation broaden when they propagate through the fiber cores, which leads to a degradation of the performances.

Importantly, both confocal detection and multiphoton excitation strategies use punctual illumination. They correspondingly require scanning and focusing mechanisms to build the final image, which both hinder miniaturization and reduce the frequency for image acquisition. Alternatively, an out-of-focus background has been rejected in non-scanning wide-field endoscopes by using structured illumination microscopy [11,19–23]. Although this approach provides wide-field images after minimal computation, it may suffer from the lack of axial optical sectioning mentioned above in confocal microscopy. Moreover, it relies on a spatial light modulator, the refreshing of which ultimately limits the frequency of image acquisition to a few hertz (Hz) [11]. Hence, due to the inherent characteristics of the bundle, the preceding methods have encountered limitations, and there is still room for alternative strategies to generate optical sectioning in fiber-bundle fluorescence endomicroscopy.

Beyond being geometrically demanding, the samples observed in fluorescence endomicroscopy often exhibit significant light scattering and autofluorescence, which are both detrimental for the quality of the image contrast. First, the biological samples may intrinsically emit fluorescence originating from endogeneous (e.g., flavins) or added (e.g., vitamins contained in culture media) components. Second, the sample may contain several fluorescent labels exhibiting spectral overlap. Eventually, the imaging fiber itself is autofluorescent, and its emission results in a significant loss of image contrast [24]. To circumvent these issues, various strategies including background subtraction [25] and un-mixing spectral analysis [26] have been proposed. However, they rely on assumptions on the autofluorescence patterns and may fail when dealing with low levels of targeted fluorescence signals with poor signal-to-noise ratios. Thus, reliable strategies to eliminate the detrimental effects of autofluorescence in fluorescence endomicroscopy are still demanded.

Among the diverse endomicroscope configurations, standard fiber-optic epifluorescence imaging with one-photon excitation is easy to use and benefits from cheap light sources and full-frame acquisition for high-speed imaging. However, it is not robust against autofluorescence and light scattering [1], and it is unable to reject the out-of-focus background (generally providing low-contrast images; see [27]). The preceding analysis prompted us to implement dynamic contrast of fluorophores in fluorescence endomicroscopy. Unlike regular fluorescence imaging, which exploits the spectral dimension to generate contrast in images, dynamic contrast discriminates reversibly photoswitchable fluorescent labels against spectrally interfering backgrounds by exploiting the dynamics of their photoswitching properties without any deconvolution or subtraction schemes [28–33]. More specifically, we adopted the fast modality of out-of-phase imaging after optical modulation (Speed OPIOM) [32,33], which uses two modulated light sources synchronized in antiphase at two wavelengths in order to drive photoswitching [Fig. 1(a)]. The Speed-OPIOM signal $\mathcal{S}$, i.e., the out-of-phase component of the modulated fluorescence signal, is directly retrieved by Fourier transform of tens to hundreds of images for at least two periods of light modulation. No further processing is necessitated and lock-in detection secures efficient noise rejection. Interestingly, $\mathcal{S}$ exhibits a narrow resonance in the space of the control parameters of illumination (light intensities and angular frequency) [Fig. 1(b)]. It is non-vanishing only when the average light intensities are tuned to maximize the photoswitching amplitude

on the changes of light intensities and the angular frequency matches with the inverse of the photoswitching relaxation time. For a given set of the control parameters of illumination, $\mathcal{S}$ exhibits as well a narrow resonance in the space of the rate
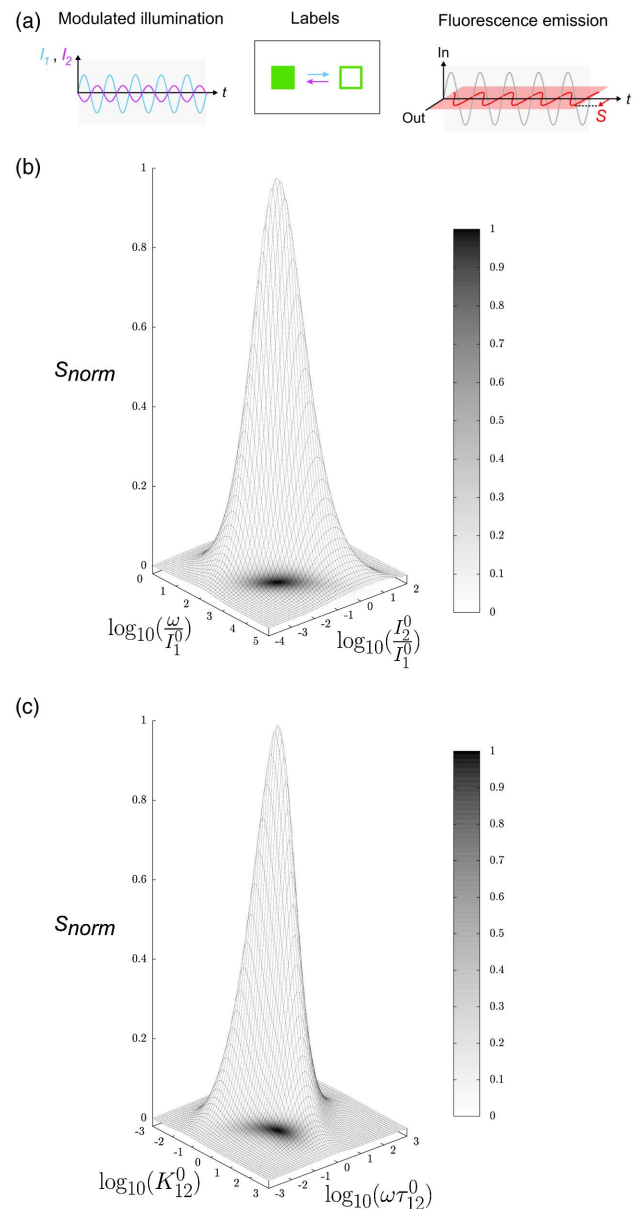
Fig. 1. (a) *Principle of Speed OPIOM*. Sinusoidally modulated light sources synchronized in antiphase at two wavelengths drive the exchange between two states of distinct brightness of reversibly photoswitchable fluorescent labels. Speed OPIOM exploits the resulting quadrature-delayed component S (in red) of their fluorescence emission. (b),(c) *Speed OPIOM for optical sectioning and selective imaging*. The normalized Speed-OPIOM signal $\mathcal{S}_{norm}$ exhibits a narrow resonance both in the space of the control parameters of illumination [(b) here parameterized by I_2^0/I_1^0 and ω/I_1^0, where I_1^0, and I_2^0, and ω respectively designate the average light intensities at both wavelengths and the angular frequency of the modulated lights] and in the space of the rate constants, which govern forward and backward photoswitching of the labels [(c) parameterized by K_{12}^0 and $\omega\tau_{12}^0$, where K_{12}^0 and τ_{12}^0 respectively designate the ratio of the average rate constants associated to forward and backward photoswitching and the photoswitching relaxation time at a steady state]. The signal level in Speed OPIOM is displayed on the gray scale at the right of each figure.

constants, which govern forward and backward photoswitching of the labels [Fig. 1(c)]. Since a reversibly photoswitchable fluorescent label has singular photochemical and kinetic properties (and correspondingly its own resonant conditions), simply tuning the illumination control parameters to its resonant values enables its selective imaging, filtering out the contribution of spectrally interfering fluorophores (non-photoswitching or non-resonant reversibly photoswitching fluorophores) as well as autofluorescence. As an additional benefit, the spatial dependence of the Speed-OPIOM resonance on the light intensities I_1^0 and I_2^0 at a given radial frequency of light modulation ω opens an unprecedented avenue to improve the axial resolution and to remove the out-of-focus fluorescence in fiber-optic epifluorescence imaging with one-photon excitation. Indeed, the spatial light profile does not exhibit a cylindrical symmetry at the fiber end (*vide infra*). As a consequence, the Speed-OPIOM resonance condition can only be met in a restricted region of space for a given set of intensities and angular frequency of the modulated light sources, which eliminates the fluorescence contributions from out-of-resonance locations.

Hence, the present paper reports on the implementation of Speed OPIOM in wide-field fluorescence endomicroscopy with one-photon excitation. We build a simple and cheap optical-fiber-bundle-based endomicroscope integrating modulatable light sources. We first demonstrate that it provides intrinsic optical sectioning, which facilitates the observation of fluorescent labels at targeted positions within the sample. Then we thoroughly evaluate its efficiency to eliminate the interference of autofluorescence arising from both the fiber bundle and the specimen when observing targeted reversibly photoswitchable fluorescent proteins (RSFPs [34]) in several biological samples. Finally, we demonstrate that it enables multiplexed observations of two spectrally similar RSFPs that differ by their photoswitching dynamics.

2. RESULTS

A. Speed-OPIOM Endomicroscope

Flexible fiber-optic-based fluorescence endomicroscopes have been mainly built around two designs [35]. In the first one, excitation light and fluorescence emission are transmitted through a single optical fiber. Scanning of the fiber over the sample allows one to collect fluorescence signals from each point of the specimen. To reconstruct the final images, one therefore needs additional micromechanical actuators to accurately drive the pathway followed by the fiber end [36–39]. In the second approach, flexible fiber bundles are used to deliver the excitation lights and send back the fluorescent images of the specimen. Although the lateral resolution is limited by the number of microfibers composing the bundle, large areas of the sample can be directly imaged without the need of scanning [40]. Our Speed-OPIOM endomicroscope exploits this second strategy with the epifluorescent fiber imaging configuration by using one-photon excitation, which enables full-frame image capture with a camera [Fig. 2(a)] [41].

To implement Speed-OPIOM imaging, the average intensities I_1^0 and I_2^0 of the excitation light modulated at angular frequency ω have to be constant over the whole imaged area and match the Speed-OPIOM resonance condition where both I_2^0/I_1^0 and ω/I_1^0 ratios are fixed. In addition, intense excitation lights should be preferentially delivered at the sample in order to increase the modulation frequency and shorten the acquisition duration. Hence, we adopted light-emitting diodes (LEDs) as light sources

since they are stable, inexpensive, easy to modulate, and suitable for the miniaturization of the device.

Our endoscope integrates two 500 mW colored LEDs with peak wavelengths at 405 and 480 nm. To insure a homogeneous illumination pattern at both wavelengths, we designed a Köhler illumination system instead of directly focusing the image of the LED chip through the objective onto the distal end of the fiber as previously described [40]. The lights emitted from the two LEDs are first collimated by a high-NA condenser, band-pass filtered, and combined together with an appropriate dichroic mirror before passing through an afocal system to provide an even illumination of circular shape thanks to a round iris. Such an illumination system is particularly suited to reduce the contributions of inhomogeneities of the LED chips and of possible misalignment between both light sources. The iris is imaged at the focal plane of a 10 × objective (NA = 0.5), where the distal end of the fiber bundle composed of 30,000 cores (average core-to-core distance of around 4.3 µm) was placed. The excitation pathway of the endoscope terminates with a needle graded-index (GRIN) lens optically cemented at the end of the fiber bundle to deport the
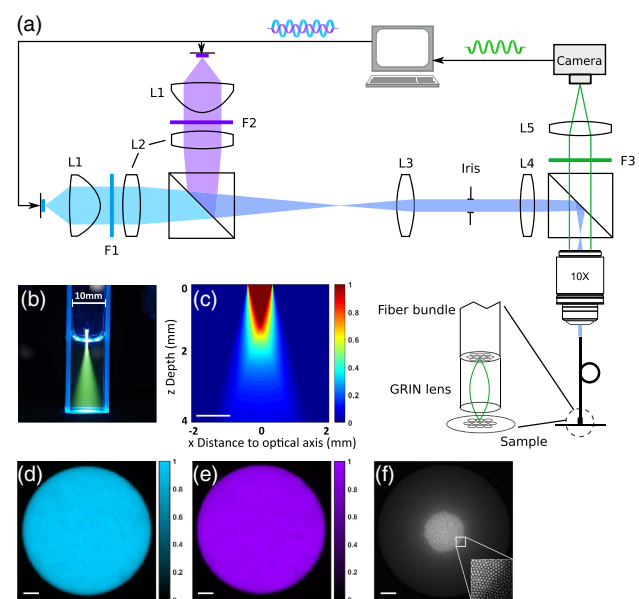
Fig. 2. *Fluorescence endoscopy setup for Speed-OPIOM imaging.* (a) Optical layout of the endoscope and its interface to a PC-based synchronized modulation and imaging acquisition system; (b) experimental light intensity profile visualized by autofluorescence of a lysogeny broth (LB) solution along the pathway of 405 nm UV light emitted from the fiber; (c) simulation of the excitation light intensity at the distal end of the fiber as a function of the sample depth. The computation was performed for a multimode fiber of 0.72 mm in diameter and 0.39 NA plunging into water ($n = 1.34$) (see Section 2 of Supplement 1). The light intensity is displayed in linear scale at the right of the image. *Scale bar*: 1 mm. (d),(e) Normalized light intensity pattern at (d) 480 nm and (e) 405 nm measured at the distal end of the fiber bundle by microscopy. A uniformity better than 90% was observed over the whole surface of the fiber bundle. The normalized light intensity is displayed in linear scale at the right of the images in (d) and (e). (f) Autofluorescence of the fiber bundle recorded under constant illumination at 480 and 405 nm upon filtering at 525 nm. The zoomed image depicts the detail of the cores and cladding giving rise to a honeycomb artifact and the slight core-to-core coupling as evidenced from detecting fluorescence in the non-illuminated cores close to the edge of the illuminated zone. *Scale bar* in (d)–(f): 100 µm.

illumination pattern over the sample at a working distance of 50 µm with a 1 × magnification.

The fluorescence image of the specimen is sent back through both the GRIN lens and the fiber bundle, and the proximal end of the bundle is further imaged by the objective. After fluorescence emission has been filtered by a band-pass filter centered at 525 nm, a tube lens permits the reconstruction of the image of the proximal end onto the CMOS sensor of a cheap camera for industrial vision, which yields a 3 × magnified image with an effective field of view of up to 790 µm in diameter. To further minimize instrument complexity and costs, modulation of lights and triggering of the acquisition by the camera are synchronized by an Arduino-compatible card (Teensy 3.5). The series of acquired fluorescence images are processed on PC by applying a time-domain Fourier transform in order to yield the time-averaged and out-of-phase images (subsequently denoted as Pre-OPIOM and Speed OPIOM, respectively), in which the honeycomb pattern from the bundle is removed by an interpolation algorithm [42] (see Section 1 and Fig. S1 in Supplement 1). It is worth noting that the Pre-OPIOM image essentially compares with the fluorescence image, which would be classically recorded under constant illumination.

B. Optical Characterization

Several measurements and theoretical computations have been performed to reveal the optical properties of our fluorescence endomicroscope. We first analyzed the emergent light at the distal end of the fiber. Figure 2(b) displays the experimental light intensity profile visualized by autofluorescence of a medium subsequently used for bacteria growth. It is axially symmetric and exhibits a conical shape. The emergent light at the distal end of the fiber has been simulated to further analyze the spatial evolution of the light intensity along the optical axis (see Section 2 of Supplement 1). Figure 2(c) shows that the light intensity remains strictly constant within a cone up to a 1.2 mm depth. It then rapidly decays both radially and along the optical axis.

We then proceeded to calibrate the light intensities delivered by the fiber bundle by analyzing the kinetics of photoswitching of two RSFPs, Dronpa-2 [43,44] and Padron [45], that we investigated in a previous study [32] (see Section 3 of Supplement 1). Although the maximum light flux transferred by the fiber bundle is limited by the low numerical aperture of a fiber core (NA = 0.39), our optimized configuration enabled us to reach a maximal irradiance of more than 10 mW/mm^2 at the distal end of the fiber. Such an irradiance allowed us to image Dronpa-2 within a few seconds with the Speed-OPIOM protocol (*vide infra*).

Figures 2(d) and 2(e) display the normalized excitation light intensities at 480 and 405 nm across the distal end of the fiber. Both light distributions exhibit excellent spatial uniformity with a fluctuation of less than 10% (see Fig. S5) in line with the Speed-OPIOM requirement discussed above. We further evaluated the dependence of the intensity and phase of the normalized excitation lights as a function of the bending of the fiber bundle (either 0 or 90°) in order to evaluate the possible impact of dynamic deformations on the Speed-OPIOM image. We did not observe any noticeable modification of the homogeneity of the intensity or of the phase over the surface of the fiber bundle when its proximal end was illuminated at 405 or 480 nm (see Fig. S6).

We eventually evidenced the fiber autofluorescence under dual illumination at 480 and 405 nm (see Section 4 of Supplement 1).

Figure 2(f) is a fluorescence image of the proximal end of the fiber by circumventing the illuminated zone to the central area of the fiber bundle. It shows that the individual microfibers are intrinsically autofluorescent, which is usually detrimental to image contrast and sensitivity.

C. Speed OPIOM to Improve Optical Sectioning in Fluorescence Endomicroscopy

To evidence the optical sectioning resulting from Speed-OPIOM implementation in fluorescence endomicroscopy with one-photon excitation, we collected the Pre-OPIOM and Speed-OPIOM signals in a series of Dronpa-2-labeled samples (see Section 5 of Supplement 1) as a function of their thickness under illumination of our endoscope, which was restricted by varying the distance z between the GRIN lens and the bottom of a quartz cuvette.

We first recorded the signals from a 1 µM Dronpa-2 solution [see Fig. 3(a)]. From 0 to 1 mm sample thickness, both Pre-OPIOM and Speed-OPIOM signals increase linearly due to the quasi-homogeneous distribution of the excitation light within a cone extending up to 1.2 mm from the focal plan [see Fig. 2(c)]. Beyond 2 mm, the light distribution exiting from the fiber bundle [see Fig. 2(c)] exhibits a significant spatial decay along the optical axis. As a consequence, the Pre-OPIOM signal increases more slowly with increasing sample depth. In contrast, the Speed-OPIOM intensity experiences more strongly the change of light intensity by departing from resonance at constant angular frequency so that the zone at lower light intensities vanishingly contribute to the Speed-OPIOM signal. Thus, beyond 2 mm, the Speed-OPIOM intensity reaches a plateau as if the Speed-OPIOM response originates from a spatially restricted section of the sample, a phenomenon that is not observed in conventional fluorescence endoscopy. These conclusions could be confirmed with numerical simulations of the Pre-OPIOM and Speed-OPIOM responses to the spatial profiles of exiting light intensity at the distal end of the fiber bundle. Figures 3(b) and 3(c) show that the Speed OPIOM response is much less spatially extended laterally and along the fiber axis than the Pre-OPIOM one, which evidences the optical sectioning provided by Speed OPIOM over an imaging protocol with constant illumination.

A similar experiment has been performed on a dense suspension of Dronpa-2-expressing bacteria. In this sample, the absorption and diffusion of the incident light further contribute to shaping the spatial profile of light intensity at the end of the fiber bundle. More specifically, absorption and diffusion introduce an attenuation length λ_c, which restricts the spatial extension of the light profile within the sample. Figure 3(d) shows that this phenomenon causes (i) the change of regime of the growth of the Pre-OPIOM signal to occur at a lower path length and (ii) the Pre-OPIOM signal to grow more slowly in the regime of large z than in the Dronpa-2 solution. It also explains that the saturation of the Speed-OPIOM signals takes place at half the distance z observed in the Dronpa-2 solution. This trend was further observed by analyzing the behavior of Dronpa-2-containing samples of increasing opacities: the larger the sample opacity, the earlier the saturation of the Speed-OPIOM signal (see Fig. S7). It was also in line with the results of numerical simulations, which demonstrated that both Pre-OPIOM and Speed-OPIOM responses are spatially less extended in the bacteria suspension than in the Dronpa-2 solution [see Figs. 3(e) and 3(f)] due to the
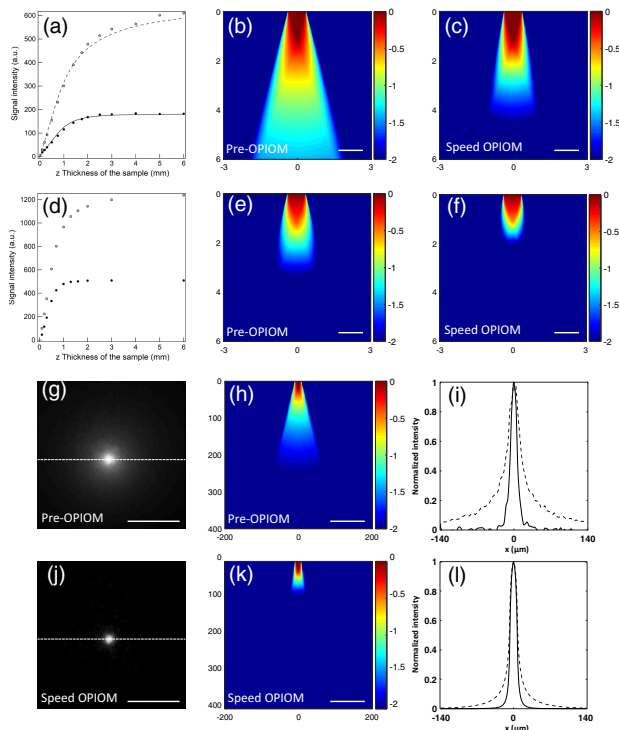
Fig. 3. *Speed OPIOM for optical sectioning.* (a),(d) Pre-OPIOM (circles) and Speed-OPIOM (disks) signals collected from (a) a 1 µm Dronpa-2 solution and (d) a dense suspension of Dronpa-2-expressing bacteria as a function of the thickness z of the sample under illumination. The Pre-OPIOM and Speed-OPIOM signals have been obtained after spatial averaging over a disk of 50 pixels (equivalent to a disk 60 µm in the sample) of the Pre-OPIOM and Speed-OPIOM images. In (a), the theoretical calculations of the Pre-OPIOM and Speed-OPIOM signals based on the simulated illumination pattern displayed in Fig. 2(c) are shown as dashed and solid lines, respectively (see Section 2 of Supporting information). (b),(e) Normalized Pre-OPIOM and (c),(f) Speed-OPIOM responses to the spatial profiles of exiting light intensity at the distal end of the fiber bundle based on the simulated illumination pattern through (b),(c) the Dronpa-2 solution and (e),(f) a scattering medium with a penetration length of $\lambda_c = 3$ mm. The signal levels in Pre-OPIOM and Speed OPIOM are displayed in common decimal logarithmic scale at the right of each image. *Axis unit:* millimeter. *Scale bar:* 1 mm. (g) Pre-OPIOM and (j) Speed-OPIOM images of 1 µm Dronpa-2 solution observed by fluorescence endomicroscopy upon illuminating a small area (a few fiber cores of the bundle; 15 µm diameter) at the proximal end of the fiber bundle. (h) Normalized Pre-OPIOM and (k) Speed-OPIOM responses to the spatial profiles of exiting light intensity at the distal end of a single microfiber based on simulated illumination pattern through the Dronpa-2 solution. The signal levels in Pre-OPIOM and Speed OPIOM are displayed in common decimal logarithmic scale at the right of each image. *Axis unit:* micrometer. (i) Experimental and (l) simulated (for an illuminated area of 15 µm diameter) signal profiles along the dashed line in (g) and (j) (dotted and solid lines correspond to Pre-OPIOM and Speed-OPIOM, respectively). *Scale bar* in (g),(h) and (j),(k): 100 µm. See Table S1 of Supplement 1 for the acquisition conditions.

attenuation length [estimated to $\lambda_c = 3$ mm from Fig. 3(d)], which further contributes to the spatial decay of the light profile.

We further explored the optical sectioning ability of the Speed-OPIOM protocol by replacing the iris in the setup shown in Fig. 2(a) with a pinhole of 150 µm diameter in order to illuminate only a small area (a few fiber cores of the bundle; 15 µm diameter) at the proximal end of the fiber bundle. The resulting point-like

source exiting the fiber was used to illuminate the 1 µM Dronpa-2 solution, and the fluorescence intensity from different locations was collected by the fiber bundle. In the corresponding Pre-OPIOM image, we observed a broad signal originating from integration of the fluorescence response over the whole illumination profile [see Fig. 3(g)]. Conversely, the signal exhibited a much narrower width in the Speed-OPIOM image, as only a restricted portion of the illumination profile generated a significant Speed-OPIOM signal [Fig. 3(j)]. The agreement between the experiment and the simulation is satisfactory for the Speed-OPIOM images. The Speed-OPIOM signal spatially decays from the center of the illumination zone as fast in the experiment as in the simulation [compare Figs. 3(i) and 3(l)]. In contrast, the measured full width at half-maximum (FWHM) is wider than the simulated one for the Pre-OPIOM signal. This discrepancy probably originates from the core-to-core coupling of the fiber bundle [see Fig. 2(f)]. The coupled cores located at a close vicinity to the illuminated ones act as secondary light sources, which both promote autofluorescence of the fiber and fluorescence of the sample so as to generate extended wings on the Pre-OPIOM peak. Since Speed OPIOM cancels out the fiber autofluorescence and requires matching of the radial frequency ω to the average light intensities I_1^0 and I_2^0, these weak secondary light sources do not generate a similar broadening of the Speed-OPIOM peak.

All together, this series of experiments suggest that Speed OPIOM can selectively enhance the in-focus fluorescence signal while minimizing the out-of-focus background fluorescence signal, which results in an improvement of axial resolution for optical sectioning.

D. Speed OPIOM to Eliminate Autofluorescence in Fluorescence Endomicroscopy

Two different series of experiments have been performed to illustrate the relevance of the Speed-OPIOM protocol to overcome the interference of autofluorescence originating from the specimen and the fiber-bundle materials, which can severely degrade image contrast in fluorescence endomicroscopy [24].

1. Sensitive Tool to Monitor Gene Expression in Bioreactors

In situ monitoring of cellular health in bioreactors is a challenge for industrial bioprocessing to ensure batch-to-batch reproducibility, maximize the yield of production, and reduce the risk of contamination associated with sampling procedures [46–48]. In addition to the measurement of metabolites in the culture medium such as O_2, CO_2, or pH, production of fluorescent proteins (FPs) such as green fluorescent protein (GFP) have been recently introduced as a reporter of the status of cells or bacteria in bioreactors, which in turn allows feedback control for the culture conditions when needed [47,49] using, e.g., optogenetic tools [50,51]. As a challenge to be tackled, the contribution of a strong autofluorescence due to both the complex nature of the culture broth and the number of fluorescent species with overlapping spectra [47] has to be quantitatively separated from the fluorescence signals of the reporter. A first proposed method was to extract the fluorescence signal of a reporting FP by subtracting the background signal obtained from a synchronized culture of non-expressing cells [52,53]. Another strategy retrieves the fluorescence signal of the reporting FP by analyzing the spectral difference between the FP and the background [54]. In addition to increasing the overall complexity of the monitoring protocol,
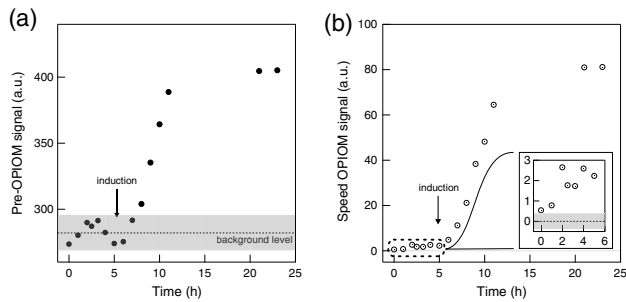
Fig. 4. *In situ* monitoring of Dronpa-2 expression in *E. coli* cultured in LB for 24 h using (a) Pre-OPIOM and (b) Speed OPIOM. In (b), the insert zooms on the 0–5 h temporal window. Spatial averaging over a disk of 50 pixels at the center of the Pre-OPIOM and Speed-OPIOM images yielded the signals represented in the figures. For each imaging protocol, the average background level and its incertitude ($\pm 1\sigma$) were measured with non-transfected *E. coli* BL21 strains cultured in LB ($n = 8$). They are displayed in the figures as dashed lines and gray areas, respectively. See Table S1 of Supplement 1 for the acquisition conditions.

both methods require high levels of reporter expression to secure sufficient signal-to-noise ratio.

Our Speed-OPIOM fluorescence endomicroscope provides an efficient and minimally invasive way to accurately sense in real time and *in situ* the production of a RSFP in a culture medium. For illustration, Dronpa-2 was expressed into *E. coli* BL21 strains under control of the lac operator (see Section 5 of Supplement 1). After cells were initially grown in LB culture at 37°C, expression of Dronpa-2 was monitored every 30 or 60 min by plunging the fiber in 2 mL of the growth medium and acquiring Pre-OPIOM and Speed-OPIOM images. It is worth noting that we fixed the optical path length between the fiber tip and the bottom of the vessel to 500 μm in order to circumscribe the influence of the optical density (OD) variation of the culture medium during cell growth. Figure 4 displays the temporal evolution of the Pre-OPIOM and Speed-OPIOM signals resulting from spatial averaging over a disk containing 50 pixels at the center of the collected images. Before induction to trigger the Dronpa-2 production by addition of isopropyl-β-D-1-thiogalactopyranoside (IPTG), it was impossible to detect the basal expression of Dronpa-2 with Pre-OPIOM since the autofluorescence arising from the fiber bundle and the culture medium [see Fig. 2(f)] exceeded the Pre-OPIOM signal from Dronpa-2 and prevented its accurate monitoring [Fig. 4(a)]. In contrast, the weak Dronpa-2 expression before induction was easily detected with Speed OPIOM [Fig. 4(b)]. Similarly, we could detect the exponential increase of the Dronpa-2 production from 6 to 12 h just after IPTG addition at 5.1 h with Speed OPIOM. Conversely, accurate monitoring of this increase required a further 3 h delay with Pre-OPIOM since Dronpa-2 fluorescence had first to emerge from the autofluorescence background. Hence, Speed OPIOM readily enlarges the dynamic range of fluorescent reporters that can be monitored by endomicroscopy. As such, it is well suited for real-time monitoring of cultures of cells even at low levels of expression of the fluorescent labels.

2. Imaging Fluorophores in Plant Roots under the Soil with Wide-Field Endomicroscopy

In a second series of experiments, we imaged the root of a living plant (*Camelina sativa* seedlings, 10 days old) directly in the soil at

a few centimeters below the surface, either ubiquituously expressing Dronpa-2 or as a wild-type specimen used as a control (see Section 5 of Supplement 1). Both plants exhibit similar Pre-OPIOM images, which results from the high level of root autofluorescence [Figs. 5(a) and 5(b)]. In particular, one cannot clearly evidence Dronpa-2 expression in the labeled plant. Furthermore, the contrast between the root and the background is poor, which originates from the significant autofluorescence of the fiber bundle. In contrast, the Speed-OPIOM images are strongly different in the labeled plant and in the wild type. The Dronpa-2-expressing root is selectively imaged with a sharp contrast against the background, as expected from elimination of the autofluorescence from the root and from the fiber bundle [Fig. 5(c)]. This outcome is confirmed by Speed-OPIOM imaging of the wild-type root, which provided a black image.

E. Multiplexed Fluorescence Imaging in Wide-Field Endomicroscopy

In addition to optical sectioning and elimination of autofluorescence, Speed OPIOM is also endowed with discriminating reversibly photoswitchable fluorophores by their photoswitching dynamics. To illustrate this attractive feature, we imaged fixed U2OS cells expressing green fluorescent proteins: two RSFPs, Dronpa-2 and Padron, tagging the cell nucleus and mitochondria, respectively, and enhanced GFP (EGFP) as a spectrally interfering fluorophore, localized at the membrane (see Section 5 of Supplement 1). In the Pre-OPIOM images, the cells could be hardly distinguished from the fluorescent background originating from the autofluorescence of the fiber bundle, which precluded the visualization of the inner structures labeled with Dronpa-2 or Padron [Figs. 6(a)–6(c)]. In contrast, Speed OPIOM efficiently cancelled out the contributions of the autofluorescence background and EGFP fluorescence. Hence, the RSFP signals could be selectively imaged with high contrast and reveal the location of
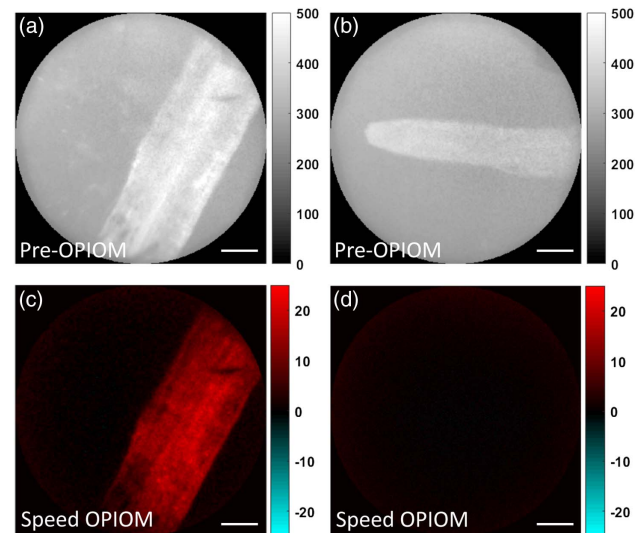

Fig. 5. *Images of Camelina sativa roots in soil obtained by fluorescence endomicroscopy.* (a),(b) Pre-OPIOM and (c),(d) Speed-OPIOM images of a root from a genetically transformed plant expressing (a),(c) Dronpa-2 or a (b),(d) wild-type plant as a control. *Scale bar:* 100 μm. See Table S1 of Supplement 1 for the acquisition conditions. The signal levels in Pre-OPIOM and Speed OPIOM are displayed in linear scale at the right of the images.

the RSFP-labeled structures. Furthermore, at Dronpa-2 resonance, the cell nuclei labeled with Dronpa-2 were unambiguously imaged, while the structures tagged with Padron were not visible [Figs. 6(d)–6(f)]. Similarly, the mitochondria labeled with Padron were selectively imaged [Figs. 6(g)–6(i)] without interference from the contribution of Dronpa-2 when the illumination parameters were tuned to Padron resonance. It is interesting to notice that the opposite signs of the Speed-OPIOM signals associated with Dronpa-2 and Padron reflected their opposite photochromic behavior: Dronpa-2 turns dark (respectively bright) upon illumination at 480 nm (respectively, 405 nm), whereas Padron becomes bright (respectively dark) upon illumination at 480 nm (respectively, 405 nm). Thus, Speed OPIOM additionally emerges as an attractive protocol for multiplexed fluorescence imaging with excellent contrast in wide-field endomicroscopy.

3. DISCUSSION

The preceding results have demonstrated that the application of the Speed-OPIOM imaging protocol considerably improves the performance of an epifluorescent fiber-bundle-based one-photon endomicroscope. Without removing any of its advantages (cheap to construct, simple to use, and enabling full- and fast-frame-rate fluorescence imaging), Speed OPIOM gives access to intrinsic optical sectioning, elimination of autofluorescence, and multiplexed observations by using a single absorption/emission channel. In the
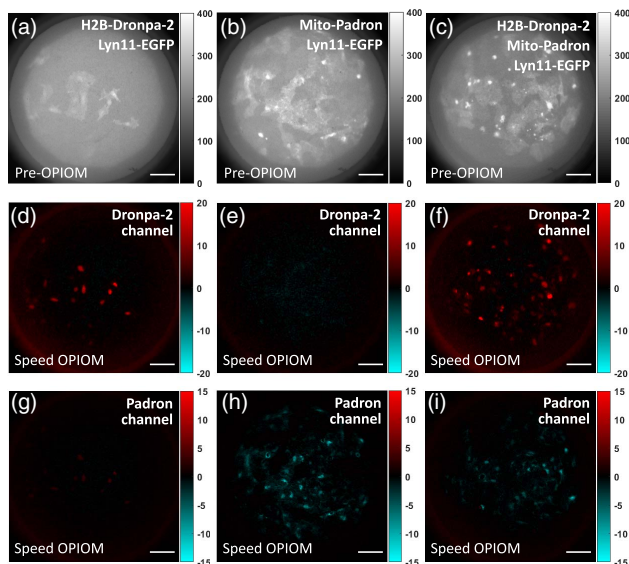
Fig. 6. *Speed OPIOM selectively discriminates RSFPs in fixed HeLa cells in the presence of a strong autofluorescent background.* (a)–(c) Pre-OPIOM images; (d)–(i) Speed-OPIOM images collected under resonance conditions for (d)–(f) Dronpa-2 and for (g)–(i) Padron. Systems: Fixed HeLa cells expressing Lyn11-eGFP tagging the cell membrane, H2B-Dronpa-2 tagging the nucleus, and Mito-Padron tagging the mitochondria as indicated in (a)–(c). (a),(d),(g) HeLa cells expressing H2B-Dronpa and Lyn11-EGFP; (b),(e),(h) HeLa cells expressing Mito-Padron and Lyn11-EGFP; (c),(f),(i) HeLa cells expressing Mito-Padron and Lyn11-EGFP. Images (e) and (g) act as negative controls to show the absence of spectral interference of (i) Padron and EGFP when using the resonance condition of Dronpa-2 and of (ii) Dronpa-2 and EGFP when using the resonance condition of Padron. The signal level in Pre-OPIOM and Speed OPIOM is displayed on the linear scale at the right of each image. *Scale bar*: 100 μm. See Table S1 of Supplement 1 for the acquisition conditions.

following paragraphs, we recapitulate its scope and limitations with respect to these issues.

In this account, we evidenced that the Speed-OPIOM observable is relevant to endow a one-photon epifluorescence endomicroscope with optical sectioning so as to significantly reduce the effective imaged volume by tuning the control parameters of illumination to resonance at the sample surface. Optical sectioning is here intrinsic and it results from applying inhomogeneous illumination on the imaged sample. Indeed, the Speed-OPIOM signal for a target is non-vanishing only when illumination fulfills two resonance conditions fixing the values of both I_2^0/I_1^0 and ω/I_1^0 ratios; the stiffer the spatial variation of I_1^0 and I_2^0, the better the optical sectioning. Chromatic aberration is limited in the fibers. Hence, the first resonance condition involving the I_2^0/I_1^0 ratio can be fulfilled over the whole inhomogeneous illumination profile and is not here significant to generate optical sectioning. In contrast, the second resonance condition involving the ω/I_1^0 ratio can only be fulfilled at a specific position of the inhomogeneous illumination profile (e.g., at the fiber tip in the present case). When the applied radial frequency ω of light modulation no longer matches its resonant value within the decaying I_1^0 and I_2^0 light profiles, the Speed-OPIOM signal is vanishing. In a fully illuminated fiber bundle, the I_1^0 and I_2^0 light profiles decay both radially and along the optical axis as shown in Fig. 2(c). The Pre-OPIOM and the Speed-OPIOM signals exhibit similar spatial evolutions over the conical volume where I_1^0 and I_2^0 are essentially constant. In contrast, the Speed-OPIOM signal spatially vanishes beyond a few millimeters along the optical axis, whereas fluorophores at higher sample depths still contribute to the Pre-OPIOM signal [see Figs. 3(b) and 3(c) and Figs. 3(a) and 3(d)]. As anticipated from its stiffer spatial profile of illumination, optical sectioning is much more efficient in a single illuminated fiber: down to 10 μm can be obtained [see Figs. 3(h) and 3(k)]. In fact, further improvements of optical sectioning capabilities of the endoscope could result from shaping the light beams emerging from the fiber to get even stiffer spatial variations of light intensities [55–58]. If one adds that Speed OPIOM easily discriminates the signal from reversible photoswitchable fluorophores from autofluorescence, optical sectioning would make our configuration of fluorescence endomicroscope especially well suited to image superficial structures [27]. Hence, one particular field of application could be imaging brain surfaces in freely moving animals, where the absence of Speed-OPIOM sensitivity to dynamical deformations would be an advantage. In fact, manipulating neural function with light and fast-frame-rate *in vivo* imaging of neural activity is becoming increasingly important [59,60]. Speed OPIOM would eliminate the fluorescence background from out-of-focus and scattered fluorescence emissions generally encountered with conventional one-photon epi-fluorescence endomicroscopy [27] [we provide further numerical simulations in Figs. S8(a)–S8(d)]. In addition, it would open an avenue to multiplexed endoscopic fluorescence observations [61] with only one wavelength channel to the most compact current setups, which are limited to imaging one genetically or anatomically defined population [59].

Speed OPIOM has demonstrated its relevance to eliminate autofluorescence as well as spectral interferences. Yet it still suffers from the limited precision on phase retrieval when extracting the out-of-phase component of the fluorescence modulation. Indeed, an error on phase retrieval will introduce into the measured signal

a contribution from the in-phase component of the fluorescence modulation, which is now partially governed by the spectral interferences. We estimate our precision to 3 10^{-3} rad range, which enables us to enhance the contrast of the targeted fluorophore against spectral interferences by a factor of 10^2–10^3. Another limitation may originate from the enhanced and intrinsic noise of the detector when the spectrally interfering signal is very strong [32]. Our equipment should presently allow us to specifically detect the OPIOM signal even in the presence of a 10^3-times-stronger non-modulated photon source.

Eventually, fluorescence endomicroscopy traditionally exploits two categories of fluorescent labels, depending on its applicative fields. Indocyanine green, Methylene blue, and Fluorescein can be presently used for clinical applications [5]. Biological applications are compatible with a broader library of fluorophores. In particular, the possibility to fluorescently tag biomolecules with absolute specificity through genetic fusion provides attractive opportunities to report on gene expression, protein trafficking, and many other dynamic biochemical pathways [62]. OPIOM has to rely on fluorophores, which exhibit reversible photoswitching under illumination when they are exposed to light. The original OPIOM protocol exploiting resonant modulated monochromatic light can be used when the backward isomerization after forward photoswitching is thermally driven [31]. Nevertheless, the Speed-OPIOM protocol [32] used in this study should be preferentially adopted when the forward and backward photoswitching processes of the reversibly photoswitchable fluorescent labels can be photochemically governed at two distinct wavelengths (e.g., in RSFPs [34], cyanines [63], and spirobenzopyrans [64]). Indeed, the Speed-OPIOM response is 2 times higher than the OPIOM one and accordingly provides a better signal-to-noise ratio. One should notice that OPIOM can also be applied to non-photoswitching fluorophores, provided that they obey a photophysical mechanism, which can be dynamically reduced to a two-state model [31]. Eventually, with respect to multiplexed observations, one should underline that Speed OPIOM can already discriminate at least four spectrally similar genetically encodable fluorescent proteins. In particular, such a state of the art would be compatible with the endoscopic analysis of populations of microorganisms (e.g., in the rhizosphere [65] or the gut) at the single-cell level in a noninvasive way.

4. CONCLUSION

In this work, we built a fiber-bundle-based fluorescent endoscopic system with modulatable one-photon excitations at two wavelengths. Upon adopting the Speed-OPIOM protocol, our cheap endoscope successively overcame the current limitations of lack of optical sectioning and autofluorescence arising from the samples or the optical components. Applying the Speed-OPIOM protocol improved sensitivity both for biomonitoring and bioimaging, as well as provided an unprecedented avenue for multiplexed fluorescent imaging. Already in the regular epifluorescence configuration, the superior performances of Speed-OPIOM imaging over conventional fluorescence are likely to find applications in diverse areas such as bioprocessing, clinical diagnostics, plant observation, and surface imaging.

See Supplement 1 for supporting content.

†These authors contributed equally to this paper.

REFERENCES

1. B. A. Flusberg, E. D. Cocker, W. Piyawattanametha, J. C. Jung, E. L. M. Cheung, and M. J. Schnitzer, "Fiber-optic fluorescence imaging," Nat. Methods **2**, 941–950 (2005).
2. J. M. Jabbour, M. A. Saldua, J. N. Bixler, and K. C. Maitland, "Confocal endomicroscopy: instrumentation and medical applications," Ann. Biomed. Eng. **40**, 378–397 (2012).
3. T. J. Muldoon, D. Roblyer, M. D. Williams, V. M. Stepanek, R. Richards-Kortum, and A. M. Gillenwater, "Noninvasive imaging of oral neoplasia with a high-resolution fiber-optic microendoscope," Head Neck Oncol. **34**, 305–312 (2012).
4. M. J. Landau, D. J. Gould, and K. M. Patel, "Advances in fluorescent-image guided surgery," Ann. Transl. Med. **4**, 392 (2016).
5. T. Nagaya, Y. A. Nakamura, P. L. Choyke, and H. Kobayashi, "Fluorescence-guided surgery," Front. Oncol. **7**, 314 (2017).
6. F. Nooshabadi, H.-J. Yang, J. N. Bixler, Y. Kong, J. D. Cirillo, and K. C. Maitland, "Intravital fluorescence excitation in whole animal optical imaging," PLoS ONE **11**, e0149932 (2016).
7. J. Vos and J. Groenwold, "Estimation of root densities by observation tubes and endoscope," Plant Soil **74**, 295–300 (1983).
8. T. K. Miriam Athmann, R. Pude, and U. Köpke, "Root growth in biopores—evaluation with in situ endoscopy," Plant Soil **371**, 179–190 (2013).
9. B. A. Flusberg, J. C. Jung, E. D. Cocker, E. P. Anderson, and M. J. Schnitzer, "In vivo brain imaging using a portable 3.9 gram two-photon fluorescence microendoscope," Opt. Lett. **30**, 2272–2274 (2005).
10. A. F. Gmitro and D. Aziz, "Confocal microscopy through a fiber-optic imaging bundle," Opt. Lett. **18**, 565–567 (1993).
11. N. Bozinovic, C. Ventalon, T. Ford, and J. Mertz, "Fluorescence endomicroscopy with structured illumination," Opt. Express **16**, 8016–8025 (2008).
12. W. Göbel, J. N. D. Kerr, A. Nimmerjahn, and F. Helmchen, "Miniaturized two-photon microscope based on a flexible coherent fiber bundle and a gradient-index lens objective," Opt. Lett. **29**, 2521–2523 (2004).
13. A. R. Rouse and A. F. Gmitro, "Multispectral imaging with a confocal microendoscope," Opt. Lett. **25**, 1708–1710 (2000).
14. J.-A. Conchello and J. W. Lichtman, "Optical sectioning microscopy," Nat. Methods **2**, 920–931 (2005).
15. P. M. Lane, A. L. P. Dlugan, R. Richards-Kortum, and C. E. MacAulay, "Fiber-optic confocal microscopy using a spatial light modulator," Opt. Lett. **25**, 1780–1782 (2000).
16. F. Jean, G. Bourg-Heckly, and B. Viellerobe, "Fibered confocal spectroscopy and multicolor imaging system for in vivo fluorescence analysis," Opt. Express **15**, 4008–4017 (2007).
17. F. Helmchen and W. Denk, "Deep tissue two-photon microscopy," Nat. Methods **2**, 932–940 (2005).
18. P. Kim, M. Puoris'haag, D. Coté, C. P. Lin, and S. H. Yun, "In vivo confocal and multiphoton microendoscopy," J. Biomed. Opt **13**, 010501 (2008).
19. S. Santos, K. K. Chu, D. Lim, N. Bozinovic, T. N. Ford, C. Hourtoule, A. C. Bartoo, S. K. Singh, and J. Mertz, "Optically sectioned fluorescence endomicroscopy with hybrid-illumination imaging through a flexible fiber bundle," J. Biomed. Opt. **14**, 030502 (2009).
20. T. N. Ford, D. Lim, and J. Mertz, "Fast optically sectioned fluorescence HiLo endomicroscopy," J. Biomed. Opt. **17**, 021105 (2012).
21. D. Xu, T. Jiang, A. Li, B. Hu, Z. Feng, H. Gong, S. Zeng, and Q. Luo, "Fast optical sectioning obtained by structured illumination microscopy using a digital mirror device," J. Biomed. Opt. **18**, 060503 (2013).

22. J. Ahn, H. Yoo, and D.-G. Gweon, "Endoscopic focal modulation microscopy," J. Microsc. **250**, 116–121 (2013).

23. P. Keahey, P. Ramalingam, K. Schmeler, and R. R. Richards-Kortum, "Differential structured illumination microendoscopy for in vivo imaging of molecular contrast agents," Proc. Natl. Acad. Sci. USA **113**, 10769–10773 (2016).

24. J. A. Udovich, N. D. Kirkpatrick, A. Kano, A. Tanbakuchi, U. Utzinger, and A. F. Gmitro, "Spectral background and transmission characteristics of fiber optic imaging bundles," Appl. Opt. **47**, 4560–4568 (2008).

25. R. Baumgartner, H. Fisslinger, D. Jocham, H. Lenz, L. Ruprecht, H. Stepp, and E. Unsold, "A fluorescence imaging device for endoscopic detection of early stage cancer—instrumental and experimental studies," Photochem. Photobiol. **46**, 759–763 (1987).

26. J. Mansfield, K. W. Gossage, C. C. Hoyt, and R. Levenson, "Autofluorescence removal, multiplexing, and automated analysis methods for in-vivo fluorescence imaging," J. Biomed. Opt. **10**, 41207 (2005).

27. J. C. Jung, A. D. Mehta, E. Aksay, R. Stepnoski, and M. J. Schnitzer, "In vivo mammalian brain imaging using one- and two-photon fluorescence microendoscopy," J. Neurophysiol. **92**, 3121–3133 (2004).

28. G. Marriott, S. Mao, T. Sakata, J. Ran, D. K. Jackson, C. Petchprayoon, T. J. Gomez, E. Warp, O. Tulyathan, H. L. Aaron, E. Y. Isacoff, and Y. Yan, "Optical lock-in detection imaging microscopy for contrast-enhanced imaging in living cells," Proc. Natl. Acad. Sci. USA **105**, 17789–17794 (2008).

29. C. I. Richards, J.-C. Hsiang, and R. M. Dickson, "Synchronously amplified fluorescence image recovery (SAFIRe)," J. Phys. Chem. B **114**, 660–665 (2010).

30. J. Widengren, "Fluorescence-based transient state monitoring for biomolecular spectroscopy and imaging," J. R. Soc. Interface **7**, 1135–1144 (2010).

31. J. Quérard, T.-Z. Markus, M.-A. Plamont, C. Gauron, P. Wang, A. Espagne, M. Volovitch, S. Vriz, V. Croquette, A. Gautier, T. Le Saux, and L. Jullien, "Photoswitching kinetics and phase-sensitive detection add discriminative dimensions for selective fluorescence imaging," Angew. Chem. Int. Ed. **127**, 2671–2675 (2015).

32. J. Quérard, R. Zhang, Z. Kelemen, M.-A. Plamont, X. Xie, R. Chouket, I. Roemgens, Y. Korepina, S. Albright, E. Ipendey, M. Volovitch, H. L. Sladitschek, P. Neveu, L. Gissot, A. Gautier, J.-D. Faure, V. Croquette, T. L. Saux, and L. Jullien, "Resonant out-of-phase fluorescence microscopy and remote imaging overcome spectral limitations," Nat. Commun. **8**, 969 (2017).

33. R. Zhang, R. Chouket, M.-A. Plamont, Z. Kelemen, A. Espagne, A. G. Tebo, A. Gautier, L. Gissot, J.-D. Faure, L. Jullien, V. Croquette, and T. L. Saux, "Macroscale fluorescence imaging against autofluorescence under ambient light," Light: Sci. Appl. **7**, 97 (2018).

34. D. Bourgeois and V. Adam, "Reversible photoswitching in fluorescent proteins: a mechanistic view," IUBMB Life **64**, 482–491 (2012).

35. G. Oh, E. Chung, and S. H. Yun, "Optical fibers for high-resolution in vivo microendoscopic fluorescence imaging," Opt. Fiber Technol. **19**, 760–771 (2013).

36. D. L. Dickensheets and G. S. Kino, "Scanned optical fiber confocal microscope," Proc. SPIE **2184**, 21849 (1994).

37. E. J. Seibel and Q. Y. Smithwick, "Unique features of optical scanning, single fiber endoscopy," Lasers Surg. Med. **30**, 177–183 (2002).

38. H. Bao, J. Allen, R. Pattie, R. Vance, and M. Gu, "Fast handheld two-photon fluorescence microendoscope with a 475 μm × 475 μm field of view for in vivo imaging," Opt. Lett. **33**, 1333–1335 (2008).

39. Y. Zhao, H. Nakamura, and R. J. Gordon, "Development of a versatile two-photon endoscope for biological imaging," Biomed. Opt. Express **1**, 1159–1172 (2010).

40. M. Pierce, D. Yu, and R. Richards-Kortum, "High-resolution fiber-optic microendoscopy for in situ cellular imaging," J. Vis. Exp. **47**, e2306 (2011).

41. C. D. Saunter, S. Semprini, C. Buckley, J. Mullins, and J. M. Girkin, "Micro-endoscope for in vivo widefield high spatial resolution fluorescent imaging," Biomed. Opt. Express **3**, 1274–1278 (2012).

42. C. Winter, T. Zerfaß, M. Elter, S. Rupp, and T. Wittenberg, "Physically motivated enhancement of color images for fiber endoscopy," in *Medical Image Computing and Computer-Assisted Intervention—MICCAI*, N. Ayache, S. Ourselin, and A. Maeder, eds. (Springer Berlin Heidelberg, 2007), pp. 360–367.

43. R. Ando, C. Flors, H. Mizuno, J. Hofkens, and A. Miyawaki, "Highlighted generation of fluorescence signals using simultaneous two-color irradiation on Dronpa mutants," Biophys. J. **92**, L97–L99 (2007).

44. A. C. Stiel, S. Trowitzsch, G. Weber, M. Andresen, C. Eggeling, S. W. Hell, S. Jakobs, and M. C. Wahl, "1.8 Å bright-state structure of the reversibly switchable fluorescent protein Dronpa guides the generation of fast switching variants," Biochem. J. **402**, 35–42 (2007).

45. M. Andresen, A. C. Stiel, J. Follig, D. Wenzel, A. Schoenle, A. Egner, C. Eggeling, S. W. Hell, and S. Jakobs, "Photoswitchable fluorescent proteins enable monochromatic multilabel imaging and dual color fluorescence nanoscopy," Nat. Biotechnol. **26**, 1035–1040 (2008).

46. A. Leung, P. M. Shankar, and R. Mutharasan, "A review of fiber-optic biosensors," Sens. Actuators B **125**, 688–703 (2007).

47. K. M. Polizzi and C. Kontoravdi, "Genetically-encoded biosensors for monitoring cellular stress in bioprocessing," Curr. Opin. Biotechnol. **31**, 50–56 (2015).

48. R. P. Harrison and V. M. Chauhan, "Enhancing cell and gene therapy manufacture through the application of advanced fluorescent optical sensors (review)," Biointerphases **13**, 01A301 (2018).

49. L. Dekker and K. M. Polizzi, "Sense and sensitivity in bioprocessing-detecting cellular metabolites with biosensors," Curr. Opin. Chem. Biol. **40**, 31–36 (2017).

50. I. Mihalcescu, M. V.-M. Gateau, B. Chelli, C. Pinel, and J.-L. Ravanat, "Green autofluorescence, a double edged monitoring tool for bacterial growth and activity in micro-plates," Phys. Biol. **12**, 066016 (2015).

51. E. M. Zhao, Y. Zhang, J. Mehl, H. Park, M. A. Lalwani, J. E. Toettcher, and J. L. Avalos, "Optogenetic regulation of engineered cellular metabolism for microbial chemical production," Nature **555**, 683–687 (2018).

52. A. Zaslaver, A. Bren, M. Ronen, S. Itzkovitz, I. Kikoin, S. Shavit, W. Liebermeister, M. Surette, and U. Alon, "A comprehensive library of fluorescent transcriptional reporters for Escherichia coli," Nat. Methods **3**, 623–628 (2006).

53. S. Berthoumieux, H. de Jong, G. Baptist, C. Pinel, C. Ranquet, D. Ropers, and J. Geiselmann, "Shared control of gene expression in bacteria by transcription factors and global physiology of the cell," Mol. Syst. Biol. **9**, 634 (2013).

54. C. A. Lichten, R. White, I. B. Clark, and P. S. Swain, "Unmixing of fluorescence spectra to resolve quantitative time-series measurements of gene expression in plate readers," BMC Biotechnol. **14**, 11 (2014).

55. U. Utzinger and R. R. Richards-Kortum, "Fiber optic probes for biomedical optical spectroscopy," J. Biomed. Opt. **8**, 121–147 (2003).

56. J. Han, M. Sparkes, and W. O'Neill, "Controlling the optical fiber output beam profile by focused ion beam machining of a phase hologram on fiber tip," Appl. Opt. **54**, 890–894 (2015).

57. G. Calafiore, A. Koshelev, F. I. Allen, S. Dhuey, S. Sassolini, E. Wong, P. Lum, K. Munechika, and S. Cabrini, "Nanoimprint of a 3d structure on an optical fiber for light wavefront manipulation," Nanotechnology **27**, 375301 (2016).

58. R. S. R. Ribeiro, P. Dahal, A. Guereiro, P. Jorge, and J. Viegas, "Optical fibers as beam shapers: from Gaussian beams to optical vortices," Opt. Lett. **41**, 2137–2140 (2016).

59. Y. Ziv and K. K. Ghosh, "Miniature microscopes for large-scale imaging of neuronal activity in freely behaving rodents," Curr. Opin. Neurobiol. **32**, 141–147 (2015).

60. W. Yang and R. Yuste, "In vivo imaging of neural activity," Nat. Methods **14**, 349–359 (2017).

61. T. J. Muldoon, M. C. Pierce, D. L. Nida, M. D. Williams, A. Gillenwater, and R. Richards-Kortum, "Subcellular-resolution molecular imaging within living tissue by fiber microendoscopy," Opt. Express **15**, 16413–16423 (2007).

62. D. M. Chudakov, M. V. Matz, S. Lukyanov, and K. A. Lukyanov, "Fluorescent proteins and their applications in imaging living cells and tissues," Physiol. Rev. **90**, 1103–1163 (2010).

63. D. P. Mahoney, E. A. Owens, C. Fan, J.-C. Hsiang, M. M. Henary, and R. M. Dickson, "Tailoring cyanine dark states for improved optically modulated fluorescence recovery," J. Phys. Chem. B **119**, 4637–4643 (2015).

64. R. Klajn, "Spiropyran-based dynamic materials," Chem. Soc. Rev. **43**, 148–184 (2014).

65. G. V. Bloemberg, A. H. M. Wijfjes, G. E. M. Lamers, N. Stuurman, and B. J. J. Lugtenberg, "Simultaneous imaging of pseudomonas fluorescence wcs365 populations expressing three different autofluorescent proteins in the rhizosphere: new perspectives for studying microbial communities," Mol. Plant-Microbe Interact. **13**, 1170–1176 (2000).